Czech Technical University
in Prague

Faculty of Nuclear Sciences and Physical
Engineering

Department of Physics

RESEARCH PROJECT

Interaction of antiproton with nuclei

Bc. Jaroslava Hrtánková

2012

Supervisor: RNDr. Jiří Mareš, CSc.

Acknowledgement

I would like to thank my supervisor, Dr. Jiří Mareš, for his assistance and useful discussions throughout writing this work.

Contents

Chapter 1

Introduction

The interaction of an antiproton with a nucleus which has been studied for decades still remains topical at present. This issue attracts much attention because it provides valuable information about the in-medium $\bar{p}N$ interaction, $\bar{p}$ behaviour in nuclear matter and about nuclear dynamics. An important aspect of this interaction is the annihilation of the antiproton in the nuclear medium. The theoretical study of the $\bar{p}$-nucleus interaction is based on an optical potential, imaginary part of which describes the antiproton absorption in a nucleus.

The experimental research of the antiproton–nucleus interaction made considerable progress with the advent of the LEAR facility at CERN in 1983, where the following processes with the antiproton beam at low energies were studied: $\bar{p}$ elastic and inelastic scattering off nuclei and proton knock-out reactions. These experimental studies provided important information about the depth of the $\bar{p}$-nucleus optical potential.

One of the very first experiments at LEAR aimed to measure the differential cross-section for the $\bar{p}$ elastic scattering off ^{12}C at 46.8 MeV [1]. The results of the measurement were in agreement with the predicted D-type potential [1, 2], with a shallow attractive real part and a deep absorptive imaginary part.

Another information about the $\bar{p}$-nucleus optical potential has been provided by antiprotonic atoms [3, 4]. In this case, the energy shifts ϵ and widths Γ of the atomic levels caused by the strong interaction has been measured. The optical potential V_{opt} in a '$t\rho$' form together with various shapes for the nuclear density distributions were used to fit 107 data points of X-ray and radiochemical data [5]. The optical potential was determined at radii where the nuclear density reaches just a few per cent of the central nuclear density. The fits led to the potential with the attractive real part about 110 MeV deep and the absorptive imaginary part about 160 MeV deep when extrapolated into the nuclear interior [5]. Such a large absorptive part

significantly suppresses the probability of penetration of the antiproton deep inside the nucleus. As a result, the $\bar{p}$ annihilation takes place at the surface region of the nucleus. Indeed, no bound states of the antiproton in a nucleus were observed so far. The question of finding the $\bar{p}$-nuclear bound states thus still remains open.

The theoretical research in this field has not stagnated, as well, and it has predicted many interesting effects concerning the interaction of the antiproton with a nucleus [6, 7, 8, 9, 10]. Bürvenich at al. [6] performed calculations of the bound antiproton in ^{16}O and ^{208}Pb within the relativistic mean-field (RMF) model. The self-consistent calculations, taking into account the rearrangement of the nuclear core, led to a strong binding of the antiproton inside the nucleus. They also revealed large compression of the nucleus induced by the presence of the antiproton. The antiproton is localized in the center of the nucleus and the density in this region reaches values 2–4 times the normal nuclear density. It is to be noted that the G-parity motivated antiproton coupling constants were used in these calculations. For the pure G-parity transformation, the total annihilation widths of $\bar{p}$ in the $^{16}O_{\bar{p}}$ system were estimated to be in the range 9–23 MeV, depending on the RMF parametrization. The corresponding lifetimes are 9–23 fm/c. Such long lifetimes are due to the suppression of the phase space available for the $\bar{p}$ annihilation at higher densities ($\sim 2\rho_0$, where $\rho_0 = 0.15$ fm^{-3}), since many of the annihilation channels are simply closed. However, larger annihilation widths are predicted by calculations with reduced $\bar{p}$ coupling constants. The predicted lifetimes in this case are in the range 1–2 fm/c.

Another approach based on the standard quantum field theory revealed a strong dependence of the annihilation probability of antibaryon in the nucleus on the effective masses of the mesons involved in the annihilation channels [11]. The contribution from the Dirac sea was considered in these calculations and it implied shorter lifetimes of an antibaryon than in the case without the Dirac sea. In other words, the annihilation is strongly suppressed at higher nuclear densities when the Dirac sea is omitted.

The dynamical transport model based on Giessen Boltzman-Uehling-Uhlenbeck (GiBUU) model [12] was used to calculate the time of the formation of a compressed $\bar{p}$-nucleus system. The GiBUU model includes relativistic mean fields for the baryons and antibaryons. The calculations revealed that it takes about 4–10 fm/c to reach the state with the maximal central density of order 2–3ρ_0 in a $\bar{p}$-nucleus system [7]. Consequently, the results of these calculations indicate that it could be possible to observe a compressed bound state of a $\bar{p}$-nucleus system.

Despite the negative results of previous experiments, it is believed that the $\bar{p}$ nuclear bound states can be detected in future measurements. The new experiment with highly energetic antiprotons of 1–15 GeV/c is planned at the FAIR facility (Darmstadt). One of its parts, the PANDA experiment [13], is going to explore the interaction of the antiprotons with nucleons and nuclei in order to study the hadron structure. These measurements are expected to provide us with new information about the $\bar{p}$N potential and $\bar{p}$ annihilation in the nuclear medium.

In my Bachelor Thesis [14], I performed calculations of the 1s1/2 $\bar{p}$ bound state in ^{16}O within the RMF model. The results of the dynamical calculations revealed that the antiproton embedded in the nucleus has a huge influence on the surrounding nucleons. A large compression of the nuclear core caused by the strongly interacting antiproton in the 1s1/2 state was observed. The central nuclear density considerably increases as a consequence of strongly attractive scalar and vector antiproton potentials, evaluated using the G-parity transformation of the nucleon coupling constants. As a consequence, the absolute values of the antiproton and nucleon single particle energies increase considerably, as well.

The aim of this work is to calculate various antiprotonic nuclei and investigate the A–dependence of the dynamical effects caused by the antiproton embedded in the nuclear medium. The interaction of the antiproton with a nucleus is described within the RMF model [15]. This work consists of 4 chapters and 1 appendix. In the second chapter, the RMF model is introduced and the equations of motion for the $\bar{p}$-nucleus system are discussed. The results of the self-consistent calculations of the $\bar{p}$ bound states in selected nuclei are discussed in Chapter 3. Conclusions are summarized in Chapter 4. The details of the calculations are presented in Appendix A.

Chapter 2

Relativistic mean-field model

In this work, the antiproton nuclear bound states are studied within the framework of the RMF model [15]. The reason for using the RMF approach is that it proved to be a suitable and efficient tool for the calculations of nuclear many-body systems. It describes successfully the ground state properties of finite nuclei [16]. Moreover, it includes naturally the antiproton into the formalism through the Dirac equation. Within this model, (anti)nucleons (and baryons, in general) are described as Dirac fields (ψ_j) and the interaction between them is mediated by meson fields which represent independent degrees-of-freedom. The formalism includes the following fields: isoscalar-scalar field $\sigma(x^\mu)$ (σ) responsible for the medium range attraction between nucleons, isoscalar-vector field $\omega_\mu(x^\mu)$ (ω) which mediates the short range repulsion, isovector-vector field $\vec{\rho}_\mu(x^\mu)$ (ρ) which allows to adjust isovector properties of nucleons, and massless vector field $A_\mu(x^\mu)$ (γ) which mediates the electromagnetic interaction. The π- and η-fields are not considered because only fields with natural parity are employed [17].

We start with the Lagrangian density for the system of nucleons and antinucleons interacting via meson fields

$$\begin{aligned}\mathscr{L} = \sum_{j=N,\overline{N}} & \bar{\psi}_j(i\gamma^\mu\partial_\mu - m_N - g_{\sigma j}\sigma - g_{\omega j}\gamma_\mu\omega^\mu - g_{\rho j}\gamma_\mu\vec{\tau}\cdot\vec{\rho}^\mu - e_j\gamma_\mu\frac{1}{2}(1+\tau_3)A^\mu)\psi_j \\ & + \frac{1}{2}\left(\partial_\mu\sigma\partial^\mu\sigma - m_\sigma^2\sigma^2\right) - \frac{1}{2}(\frac{1}{2}\Omega_{\mu\nu}\Omega^{\mu\nu} - m_\omega^2\omega^\mu\omega_\mu) \\ & - \frac{1}{2}(\frac{1}{2}\vec{R}_{\mu\nu}\cdot\vec{R}^{\mu\nu} - m_\rho^2\vec{\rho}_\mu\cdot\vec{\rho}^\mu) - \frac{1}{4}F_{\mu\nu}F^{\mu\nu} \\ & - \frac{1}{3}g_2\sigma^3 - \frac{1}{4}g_3\sigma^4 + \frac{1}{4}d(\omega^\mu\omega_\mu)^2,\end{aligned} \tag{2.1}$$

where the arrow denotes an isovector quantity and $\vec{\tau}$ is the triplet of Pauli matrices; m_N is the mass of the (anti)nucleon, m_σ, m_ω, m_ρ are the masses of the σ-, ω- and ρ-meson; $g_{\sigma j}$, $g_{\omega j}$, $g_{\rho j}$ and e_j are the coupling constants of the corresponding fields

with the (anti)nucleon. The field tensors $G_{\mu\nu}$ of the vector fields ($G = \Omega, \vec{R}, F$) are defined as:

$$G_{\mu\nu} = \partial_\mu G_\nu - \partial_\nu G_\mu \ . \tag{2.2}$$

The model is based on the *mean-field* and *no-sea* approximations [17]. The former means that the meson fields are treated as classical c-number fields. The quantum fluctuations are eliminated by averaging the meson fields contributions and thus the nucleons move as an independent particles in the common mean-field. The *no-sea* approximation consists in omitting the contribution from vacuum polarization. It means that we neglect the contribution of antiparticles and we take into account only the contribution of A nucleons in the nucleus. Further, we look for the stationary solution and assume spherically symmetric nuclei. This implies that all time derivatives of the fields will be zero and all spatial components of the fields will be zero, as well. Therefore, only the fields σ, ω_0, ρ_0 and A_0 remain after the above simplifications. Using the Hamilton´s variational principle we derive the equations of motion for the system of interacting nucleons and an antiproton. The Dirac equation for the antiproton and nucleons reads

$$[-i\vec{\alpha}\vec{\nabla} + \beta(m_N + S_j) + V_j]\psi_j^\alpha = \epsilon_j^\alpha \psi_j^\alpha, \tag{2.3}$$

where

$$S_j = g_{\sigma j}\sigma, \quad V_j = g_{\omega j}\omega_0 + g_{\rho j}\rho_0\tau_3 + e_j\frac{1+\tau_3}{2}A_0,$$

end α denotes various single particle states. The Klein-Gordon equations for the meson fields are as follows:

$$\begin{aligned}
(-\triangle + m_\sigma^2 + g_2\sigma + g_3\sigma^2)\sigma &= -\sum_j g_{\sigma j}\rho_{Sj} \\
(-\triangle + m_\omega^2 + d\omega_0^2)\omega_0 &= \sum_j g_{\omega j}\rho_{Vj} \\
(-\triangle + m_\rho^2)\rho_0 &= \sum_j g_{\rho j}\rho_{Ij} \\
-\triangle A_0 &= \sum_j e_j\rho_{Qj},
\end{aligned} \tag{2.4}$$

where $\rho_{Sj}, \rho_{Vj}, \rho_{Ij}$ and ρ_{Qj} are the scalar, vector, isovector and charge densities,

respectively, defined as

$$\rho_{Sj} = \sum_{\alpha=1}^{A} \bar{\psi}_j^\alpha \psi_j^\alpha \tag{2.5}$$

$$\rho_{Vj} = \sum_{\alpha=1}^{A} \bar{\psi}_j^\alpha \beta \psi_j^\alpha \tag{2.6}$$

$$\rho_{Ij} = \sum_{\alpha=1}^{A} \bar{\psi}_j^\alpha \beta \tau_3 \psi_j^\alpha \tag{2.7}$$

$$\rho_{Qj} = \sum_{\alpha=1}^{A} \bar{\psi}_j^\alpha \beta \frac{1+\tau_3}{2} \psi_j^\alpha, \tag{2.8}$$

where the sums run over all occupied single-particle states α. The system of coupled equations (2.3) and (2.4) for nucleons, antiproton and meson mean fields was solved self-consistently using an iterative procedure. The numerical solution is described in detail in Appendix A. The requirement of self-consistency appeared crucial for the proper evaluation of the dynamical effects of the antiproton on the nuclear core and vice versa.

The total binding energy of the system containing A nucleons and one antiproton reads:

$$\begin{aligned} -E_B &= E + E_{CMS} - A m_N - m_{\bar{p}} \\ &= \textstyle\sum_{\alpha=1}^{A} (\epsilon_\alpha - m_N) + (\epsilon_{\bar{p}} - m_{\bar{p}}) \\ &- \frac{1}{2} \int \mathrm{d}^3x \, (-g_{\sigma N}\, \sigma \rho_S + g_{\omega N}\, \omega_0 \rho_V + g_{\rho N}\, \rho_0 \rho_I + e\, A_0 \rho_p) \\ &- \frac{1}{2} \int \mathrm{d}^3x \, (-\tfrac{1}{3} g_2\, \sigma^3 - \tfrac{1}{2} g_3\, \sigma^4 + \tfrac{1}{2} d\, \omega^4) \\ &- \frac{1}{2} \int \mathrm{d}^3x \, (-g_{\sigma\bar{p}}\, \sigma \rho_{S\bar{p}} + g_{\omega\bar{p}}\, \omega_0 \rho_{V\bar{p}} + g_{\rho\bar{p}}\, \rho_0 \rho_{I\bar{p}} - e\, A_0 \rho_{\bar{p}}) \\ &- 30.75 \; (A+1)^{-1/3} [\mathrm{MeV}], \end{aligned} \tag{2.9}$$

where E_{CMS} is the center-of-mass energy. Another useful quantity describing the nuclear properties is the root mean square (RMS) radius

$$r_{RMS} = \sqrt{\int_V r^2 \psi^\dagger \psi dV}. \tag{2.10}$$

2.1 Parametrization used in the RMF model

The parameters for the RMF model which appear in the Lagrangian density (2.1) are determined phenomenologically. There exist several sets of parameters which were obtained by fitting the nuclear matter properties and the binding energies and rms radii of selected nuclei. In our calculations, we used the linear HS [18] and nonlinear TM1 and TM2 [19] parameter sets (the TM1 model is used for heavy nuclei while the TM2 parametrization is used for light nuclei). The parameters of the RMF models applied in this work are quoted in Table.2.1.

Table 2.1: The parameters of the TM1, TM2 and HS model

	TM1	TM2	HS
m_N[MeV]	938	938	939
m_σ [MeV]	511.198	526.443	520
m_ω [MeV]	783	783	783
m_ρ [MeV]	770	770	770
$g_{\sigma N}$	10.0289	11.4694	10.47
$g_{\omega N}$	12.6139	14.6377	13.8
$g_{\rho N}$	9.2644	9 .3566	8.07
g_2 [fm^{-1}]	-7.2325	-4.444	0
g_3	0.6183	4.6076	0
d	71.3075	84.5318	0

Chapter 3

Results and discussion

We performed static as well as dynamical self-consistent RMF calculations of various nuclei with the antiproton bound in the 1s1/2 state. The examined systems were ^{16}O+$\bar{p}$, ^{40}Ca+$\bar{p}$ and ^{90}Zr+$\bar{p}$. We focused primarily on a detailed study of the effects caused by the antiproton embedded in these nuclear systems. We calculated nuclear binding energies, nucleon and $\bar{p}$ density distributions, rms radii, and single particle energies.

The potential for the antiproton could be in principle obtained by the G-parity transformation of the nucleon couplings to the meson fields involved. This transformation leaves the nucleon couplings to the σ and ρ mesons unchanged while the coupling to the ω meson changes its sign. The following relationships between the $\bar{p}$ and proton coupling constants then hold:

$$g_{\sigma\bar{p}} = g_{\sigma N}, \quad g_{\omega\bar{p}} = -g_{\omega N}, \quad g_{\rho\bar{p}} = g_{\rho N} \ . \tag{3.1}$$

Such an antiproton potential becomes very strongly attractive, without repulsion at short distances. However, the experiments with antiprotons revealed that the $\bar{p}$ potential differs significantly from that one obtained by the exact G-parity transformation. This deviation may be caused by many-body effects and annihilation of the antiproton in the nucleus [6]. Therefore, we apply also the reduced antiproton coupling constants

$$g_{\sigma\bar{p}} = \xi\, g_{\sigma N}, \quad g_{\omega\bar{p}} = -\xi\, g_{\omega N}, \quad g_{\rho\bar{p}} = \xi\, g_{\rho N} \ , \tag{3.2}$$

where the parameter ξ is considered to have the same value for all fields from interval $\langle 0, 1\rangle$. To be more specific, we used the values $\xi = 0.25, 0.5, 0.75, 1$ in our calculations.

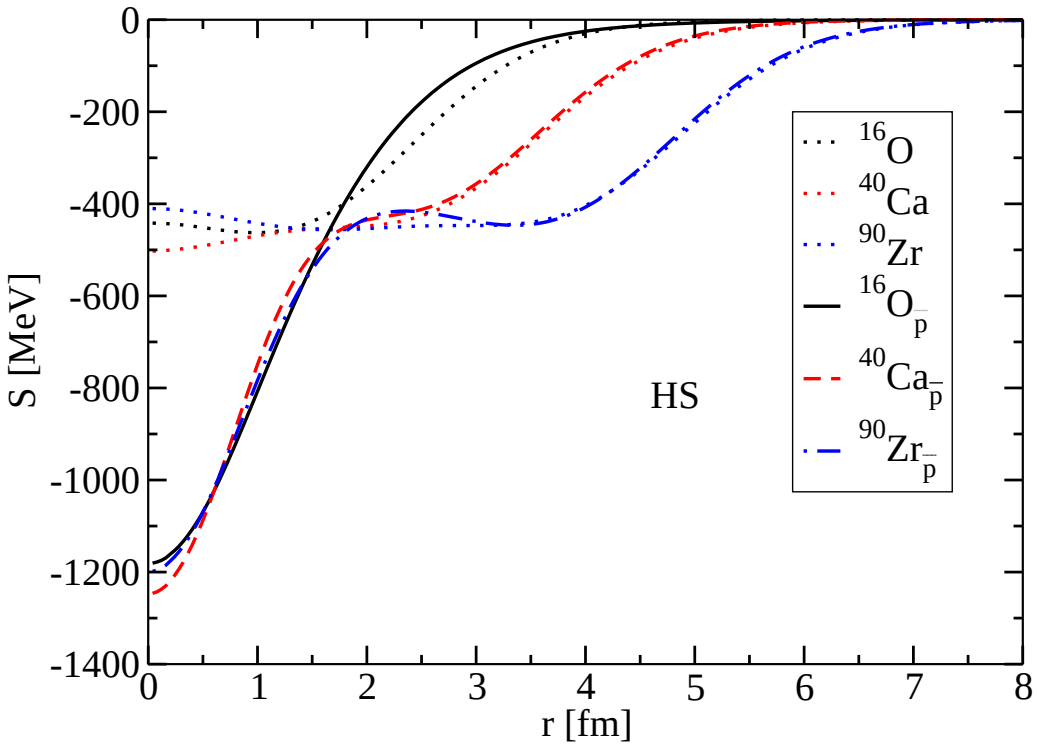

Figure 3.1: The scalar potential felt by the antiproton in $^{16}O_{\bar{p}}$, $^{40}Ca_{\bar{p}}$, $^{90}Zr_{\bar{p}}$, calculated for $\xi = 1$ in the HS model. The scalar potential for nucleon in ^{16}O, ^{40}Ca, ^{90}Zr is shown for comparison (dotted lines).

In Fig. 3.1, the scalar potential for the antiproton is shown for the systems $^{16}O_{\bar{p}}$, $^{40}Ca_{\bar{p}}$, and $^{90}Zr_{\bar{p}}$, calculated for $\xi = 1$ within the HS model. We can observe a huge increase of the potential depth when compared with the nucleon potential in normal nuclei. However, this significant change takes place only just in the central region up to ~ 1.5 fm. At larger distances, the shape of the potential is almost unchanged, especially for heavier nuclei such as ^{40}Ca and ^{90}Zr. This behaviour of the potential is connected with the density distribution of the antiproton in the nucleus, as can be seen in Fig. 3.4. Here, the antiproton is localized near the center of the nucleus (r <1.5 fm), which corresponds to the region where the scalar potential significantly increases. The depth of the potential is approximately the same for all mentioned nuclei, in accord with small variations of the central densities. It is to be noted that in the RMF model, densities and potentials are connected to each other via the system of Klein-Gordon and Dirac equations, see equations (2.3),(2.4).

The vector potentials for the antiproton in $^{16}O_{\bar{p}}$, $^{40}Ca_{\bar{p}}$, and $^{90}Zr_{\bar{p}}$ are shown in Fig. 3.2, calculated for $\xi = 1$ within the HS model. The $\bar{p}$ vector potential becomes attractive due to the G-parity transformation. The vector potentials for nucleons in ^{16}O, ^{40}Ca, and ^{90}Zr are presented with inverse sign for comparison. The change of the depth of the vector potential for $\bar{p}$ is again restricted to the central region. Since

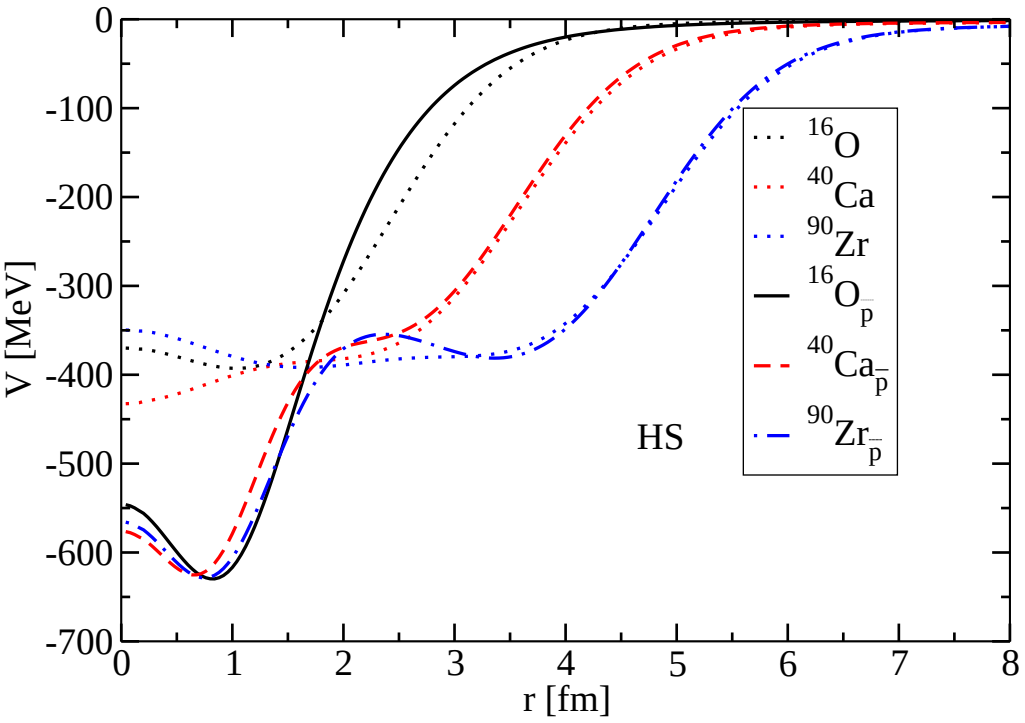

Figure 3.2: The vector potential felt by the antiproton in $^{16}O_{\bar{p}}$, $^{40}Ca_{\bar{p}}$, $^{90}Zr_{\bar{p}}$, calculated for $\xi = 1$ in the HS model. The vector potential for nucleon in ^{16}O, ^{40}Ca, ^{90}Zr with inverse sign is shown for comparison (dotted lines).

both the scalar and the vector potentials for $\bar{p}$ are attractive, the antiproton will be deeply bound in the nucleus. It will strongly attract the surrounding nucleons and this will be realized particularly in the central region of the nucleus.

In Fig. 3.3, the comparison between nucleon densities in a $\bar{p}$-nucleus and an ordinary nucleus is displayed for $^{16}O_{\bar{p}}$, $^{90}Zr_{\bar{p}}$ and ^{16}O, ^{90}Zr. The densities are calculated for $\xi = 1$ within the HS model. A large increase of the core density is obvious in both antiprotonic nuclei — the density in $^{16}O_{\bar{p}}$ and $^{90}Zr_{\bar{p}}$ reaches about 3 times the normal nuclear density. The antiproton embedded in the nucleus causes its compression. This effect is more significant in the case of $^{16}O_{\bar{p}}$ where the whole nucleus is affected by the presence of the antiproton. In the case of $^{90}Zr_{\bar{p}}$, the change in the nucleon density distribution is noticeable only in the central region of the nucleus, thus following the sizeable increase of the $\bar{p}$ potential depth. The nucleon density remains almost unchanged at larger distances from the center where the nucleons do not feel such strong attraction from the antiproton. Consequently, the depth of the $\bar{p}$ potential in this region is the same as for nucleons in $^{90}Zr_{\bar{p}}$ (compare Fig.3.1 and 3.2, where the vector potential in ordinary nucleus is with opposite sign).

In Fig. 3.4, we can observe the density distribution of nucleons in $^{16}O_{\bar{p}}$, $^{40}Ca_{\bar{p}}$ and $^{90}Zr_{\bar{p}}$, calculated for $\xi = 1$ within the HS model. The antiproton density is shown for given nuclei too. As we can see, the antiproton is localized in the central

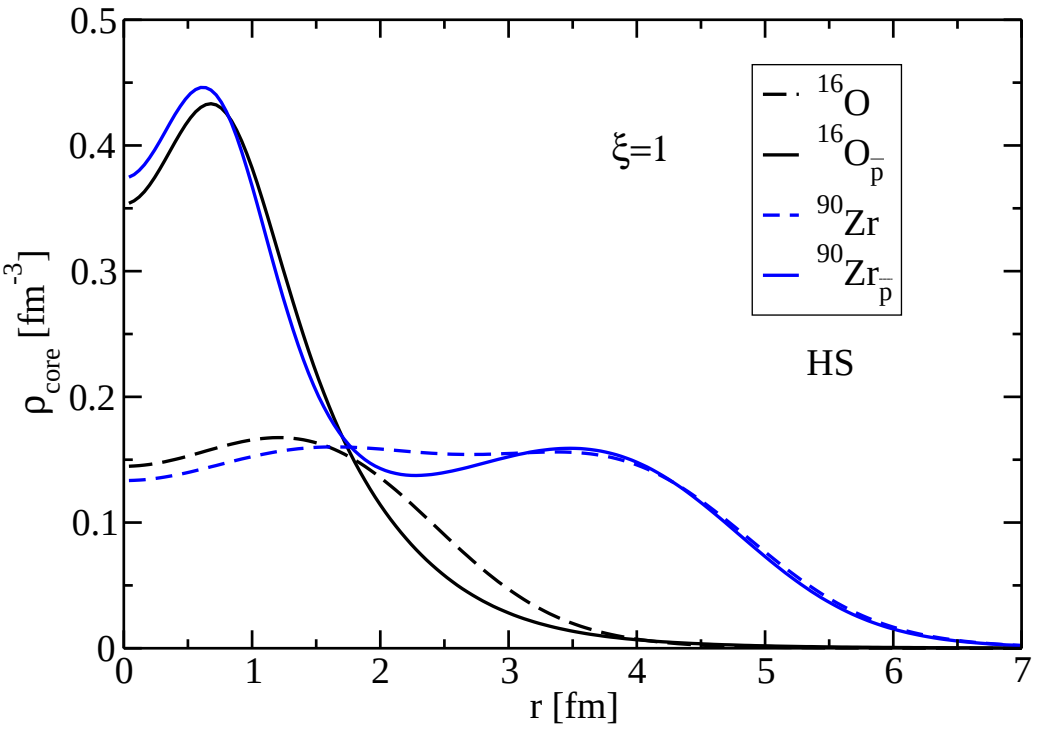

Figure 3.3: The density of nucleons in $^{16}O_{\bar{p}}$ and $^{90}Zr_{\bar{p}}$ are compared with the densities in ^{16}O and ^{90}Zr. The densities are calculated for $\xi = 1$ within the HS model.

region of each nucleus up to ∼1.5 fm. We can observe the corresponding increase in the nucleon density distribution in this region. The nucleons are gathering around the antiproton as they feel strong attraction.

The difference between the proton and neutron densities in $^{90}Zr_{\bar{p}}$ is displayed in Fig. 3.5 for various values of ξ calculated within the HS model. A similar effect was observed in $^{16}O_{\bar{p}}$, which was published in ref.[14]. For all considered values of ξ, the density of protons in the central region is higher than the density of neutrons. The difference between the proton and neutron density first increases with the increasing value of parameter ξ and saturates at the value $\xi = 0.5$, when the antiproton density saturates as well. This saturation might be the result of an increasing influence of more distant nucleons. As the interaction force of the antiproton on these nucleons increases, so does the influence of the nucleons on the antiproton and the antiproton is then pulled by these nucleons. As a consequence, the density of the antiproton decreases in the central region and spreads over a larger region. The p-n density difference starts to agree with $\triangle\rho = \rho_p - \rho_n$ in the ordinary nucleus ^{90}Zr around 2 fm. Again, the rearrangement of the nucleons is restricted to the central region of the nucleus.

In Fig. 3.6, the single particle energies of protons and neutrons are displayed for the $^{40}Ca_{\bar{p}}$ system, calculated for $\xi = 1$ within the TM1 model. Protons feel the

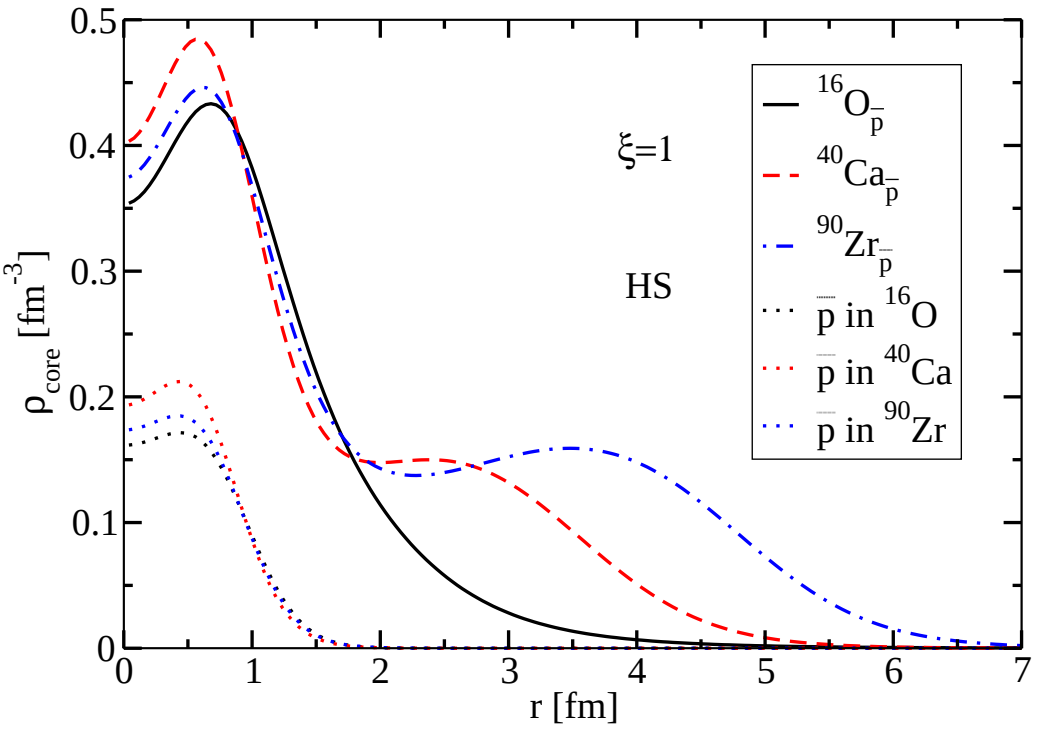

Figure 3.4: The nucleon and antiproton densities in $^{16}O_{\bar{p}}$, $^{40}Ca_{\bar{p}}$, $^{90}Zr_{\bar{p}}$, calculated for $\xi = 1$ within the HS model.

isovector and Coulomb attraction due to the antiproton and, therefore, they are more bound than neutrons, which feel the isovector repulsion. The proton and neutron single particle states 1s1/2 and 2s1/2 are bound in $^{40}Ca_{\bar{p}}$ much more strongly than in ^{40}Ca while the other nucleon levels are not so much affected by $\bar{p}$. The spin-orbit splitting of the p and d levels is larger than in the ordinary nucleus. It is proportional to the sum of the absolute values of the scalar and vector potentials (this follows from the nonrelativistic reduction of the Dirac equation), which is larger in a nucleus with $\bar{p}$ than in a normal nucleus. Consequently, the 1p1/2 and 1d3/2 levels are shifted upward and are bound less than in ^{40}Ca. When the antiproton is embedded in the nucleus, the potential well for nucleons becomes deeper and narrower than in the case of ^{40}Ca and, therefore, the level spacing between the s and p levels increases, as witnessed in Fig. 3.6.

In Fig. 3.7, the single particle energies are displayed in $^{90}Zr_{\bar{p}}$, calculated for $\xi = 1$ within the HS model. In this case, the energies of the proton and neutron 1s1/2 levels reach almost the same values. The proton repulsion could be the reason why the protons are not bound much strongly as was the case of $^{40}Ca_{\bar{p}}$. Namely, there are more protons in $^{90}Zr_{\bar{p}}$ than in $^{40}Ca_{\bar{p}}$ so the effect of repulsion is bigger and, therefore, protons in 1s1/2 state are less bound in $^{90}Zr_{\bar{p}}$ than in $^{40}Ca_{\bar{p}}$. On the other hand, neutrons in 1s1/2 are more bound in $^{90}Zr_{\bar{p}}$ than in $^{40}Ca_{\bar{p}}$. The spin-orbit

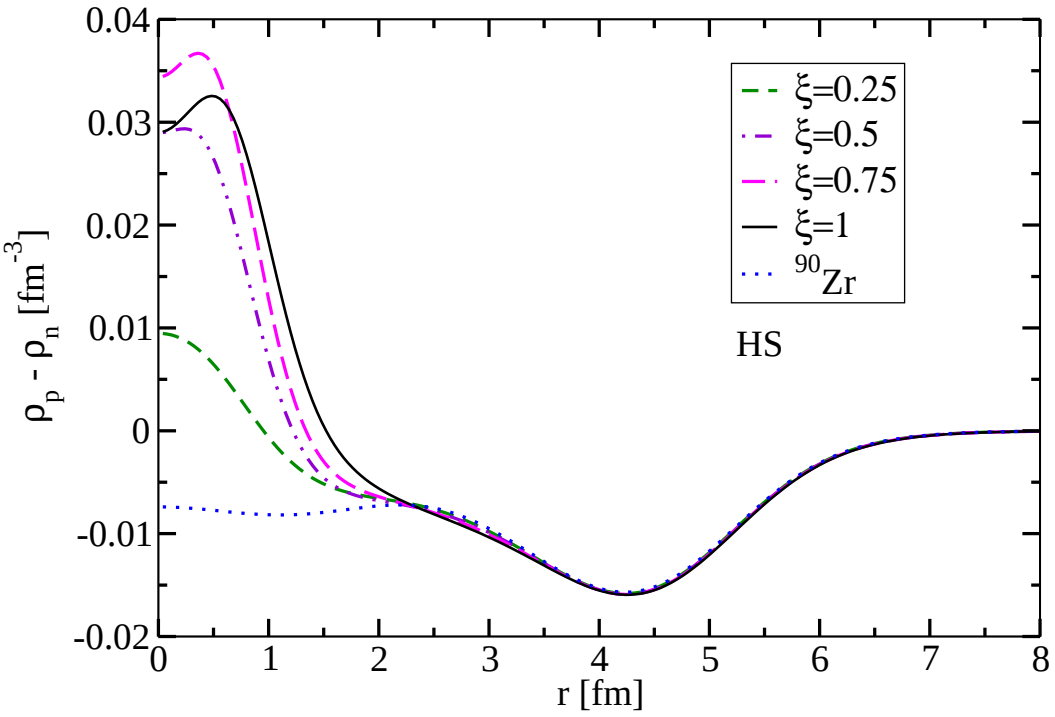

Figure 3.5: The difference between the proton and neutron densities $\triangle\rho = \rho_p - \rho_n$ in $^{90}Zr_{\bar{p}}$, calculated for different values of the parameter ξ within the HS model. The case of ^{90}Zr (dotted line) is shown for comparison.

splitting of p, d and f levels is again larger than in ordinary ^{90}Zr. As a consequence, the energy levels in $^{90}Zr_{\bar{p}}$ are rearranged due to this larger splitting.

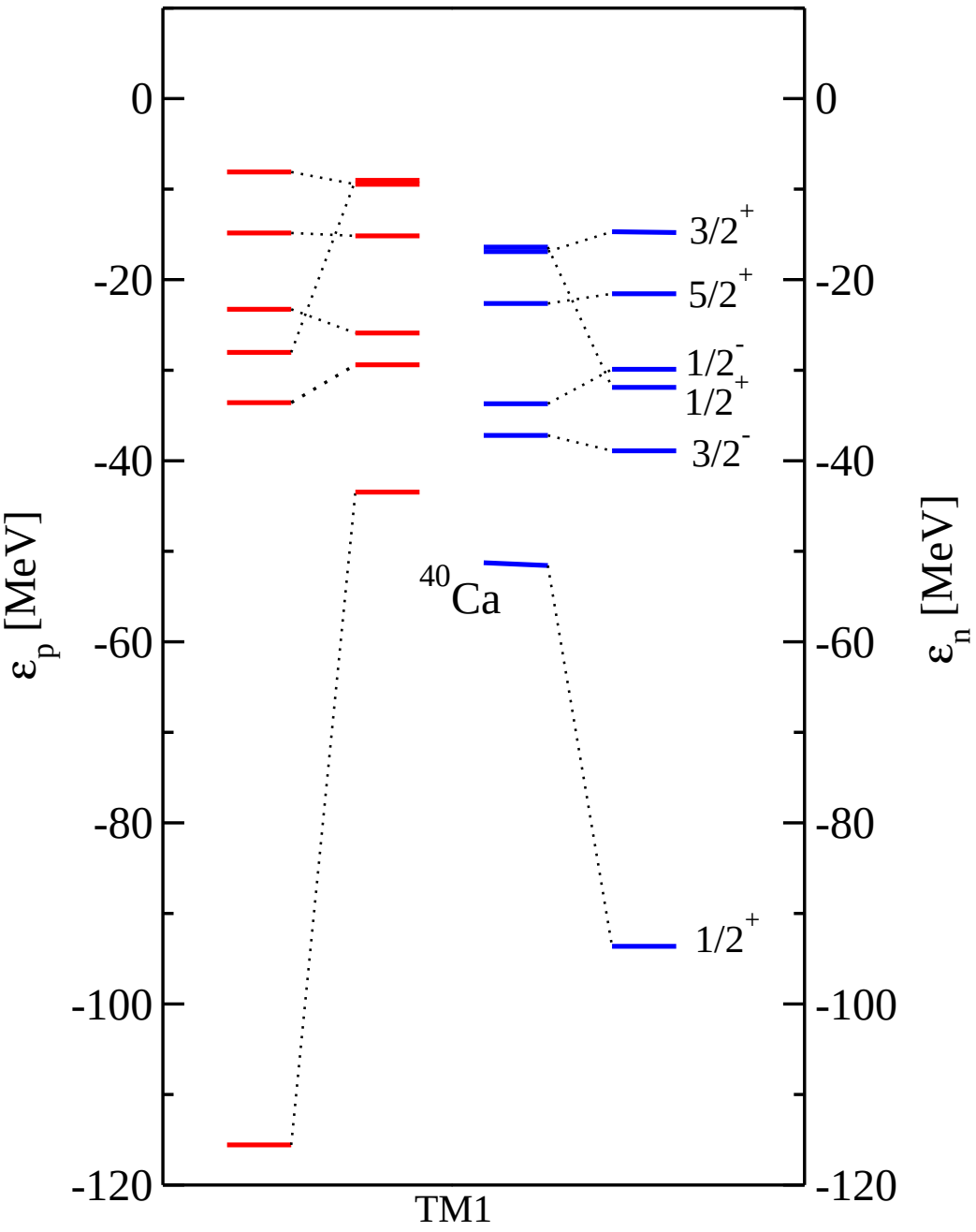

Figure 3.6: The single particle energies of protons (red) and neutrons (blue) in $^{40}\mathrm{Ca}_{\bar{p}}$ and single particle energies in ^{40}Ca, calculated for $\xi = 1$ within the TM1 model.

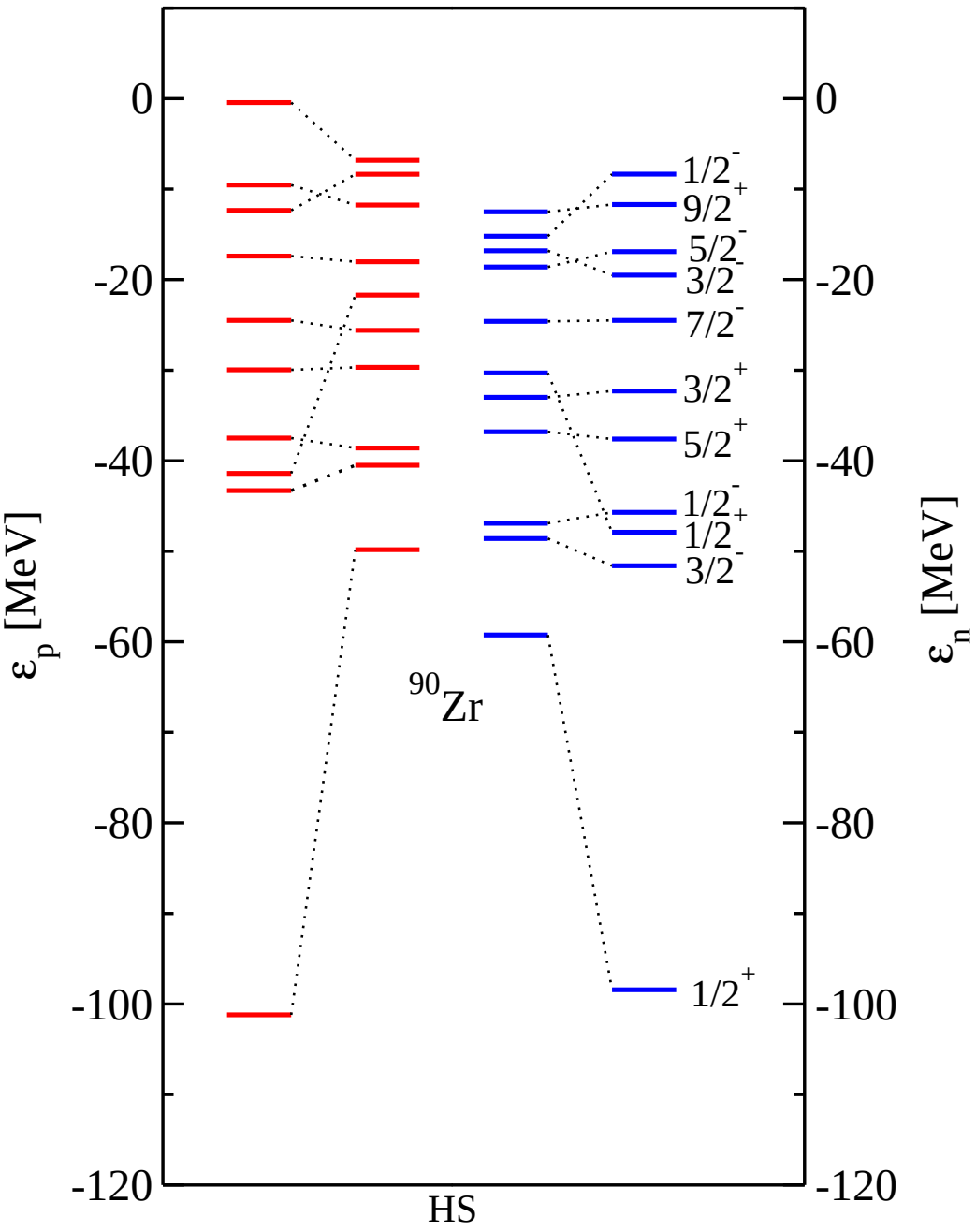

Figure 3.7: The single particle energies of protons (red) and neutrons (blue) in $^{90}\mathrm{Za}_{\bar{p}}$ and single particle energies in ^{90}Zr, calculated for $\xi = 1$ within the HS model.

Table 3.1: Binding energies B and the antiproton 1s-state single particle energies $E_{\bar{p}}$ for $^{16}O_{\bar{p}}$, $^{40}Ca_{\bar{p}}$ and $^{90}Zr_{\bar{p}}$ calculated dynamically within the HS model. Binding energies of normal nuclei are shown for comparison in parentheses.

	B [MeV]	$E_{\bar{p}}$ [MeV]
^{16}O	1247.2 (90.2)	-1240.8
^{40}Ca	1412.8 (260.2)	-1218.1
^{90}Zr	1783.8 (635.7)	-1236.6

Table 3.2: Binding energies B and the antiproton 1-s state single particle energies $E_{\bar{p}}$ for $^{16}O_{\bar{p}}$ calculated dynamically within the TM2 model and $^{40}Ca_{\bar{p}}$ calculated dynamically within the TM1 model. Binding energies of normal nuclei are shown for comparison in parentheses.

	B [MeV]	$E_{\bar{p}}$ [MeV]
^{16}O	1259.9 (128.6)	-1212.4
^{40}Ca	1364.3 (344.4)	-1097.2

In Table 3.1, we present the total binding energies and $\bar{p}$ single particle energies for $^{16}O_{\bar{p}}$, $^{40}Ca_{\bar{p}}$ and $^{90}Zr_{\bar{p}}$, calculated for $\xi = 1$ within the HS model. In Table 3.2, the same quantities are shown for the TM1 and TM2 models. The binding energy of the nuclear systems with the bound antiproton is considerably increased. However, the difference between the binding energy of the $\bar{p}$ nucleus and the normal nucleus is decreasing with increasing mass number, for both the TM and HS models. This trend is connected with the decreasing polarization of the nucleus as A increases. The $\bar{p}$ single particle energies have an interesting behavior: the depth of the $\bar{p}$ potential within the HS model reaches the value of -1726.7 MeV, -1822.7 MeV and -1764.4 MeV in $^{16}O_{\bar{p}}$, $^{40}Ca_{\bar{p}}$ and $^{90}Zr_{\bar{p}}$ respectively. On the other hand, the absolute value of the $\bar{p}$ 1s-state single particle energy is largest (smallest) for $^{16}O_{\bar{p}}$ ($^{40}Ca_{\bar{p}}$). The same situation holds for the TM model. We would expect that the deepest potential well would correspond to the most bound antiproton. Actually, it seems that not only the depth of the $\bar{p}$ potential but also its range is important. The central $\bar{p}$ potential has slightly larger range in $^{16}O_{\bar{p}}$ than in $^{40}Ca_{\bar{p}}$ and $^{90}Zr_{\bar{p}}$ in the region of the most significant increase of the potential depth, as can be seen in figures 3.1 and 3.2. The order of the potential range from the biggest to the smallest is $^{16}O_{\bar{p}}$, $^{90}Zr_{\bar{p}}$ and $^{40}Ca_{\bar{p}}$ which corresponds to the order of the absolute values of the $\bar{p}$ single particle energies.

Chapter 4

Summary

In the present work, the antiproton–nucleus bound states were studied with the aim to examine the influence of the antiproton on nucleons in nuclei across the periodic table. We performed dynamical calculations of the antiproton bound in the 1s1/2 state of $^{16}O_{\bar{p}}$, $^{40}Ca_{\bar{p}}$ and $^{90}Zr_{\bar{p}}$ within the relativistic mean-field approach. We used the linear HS model and the nonlinear TM1 and TM2 models in the calculations. The antiproton coupling constants were obtained by the G-parity transformation of the nucleon coupling constants to the meson fields. Possible deviations of the $\bar{p}$-meson couplings for the G-parity values were taken into account by introducing a scaling factor. In calculations, we focused on the antiproton potential, single particle energies and densities as well as the nucleon density distributions and single particle energies.

The insertion of the antiproton into the nucleus causes significant changes in the nuclear structure. We observed a considerable increase of the depth of the $\bar{p}$ scalar and vector potentials in comparison with the depth of the corresponding nucleon potential in ordinary nuclei (where the vector potential was taken with opposite sign). However, the increase is remarkable only in the central region of the nucleus (r<1.5 fm) and the depth of the $\bar{p}$ potential is approximately the same for all nuclei. The nucleon densities reach about 3 times the normal nuclear density in all nuclear systems with $\bar{p}$. The increase is again restricted to the central region of each nucleus and corresponds with the localization of the antiproton in nuclei. While the nucleus $^{16}O_{\bar{p}}$ is affected as a whole by the presence of the antiproton, in the case of heavier nuclei such as ^{40}Ca and ^{90}Zr, the polarization effects are significant only in the central region of these nuclei while the rest of them remains unchanged. This implies that the polarization effects in a nucleus caused by the antiproton decrease with increasing A.

The nucleon single particle energies are affected by the antiproton as well. The largest changes leading to much deeper binding were observed for the 1s1/2 and

2s1/2 levels. The spacing between the s and p levels increases because of the deeper and narrower potential well for nucleons in the $\bar{p}$ nucleus. Due to the larger spin-orbit splitting, the level ordering is rearranged in $^{40}\mathrm{Ca}_{\bar{p}}$ and $^{90}\mathrm{Zr}_{\bar{p}}$.

The nuclear binding energies of all systems with $\bar{p}$ increase significantly in both RMF models. An interesting behavior of the $\bar{p}$ single particle energies as function of A was observed. The absolute values of the $\bar{p}$ single particle energies of the order of 1000 MeV do not simply increase with increasing depth of the $\bar{p}$ potential since they depend on the radial shape of the potential, as well.

It is to be noted that the annihilation of the antiproton in the nuclear medium was not considered in our calculations. In further studies, we are about to include the absorption of the $\bar{p}$ in the nucleus in the calculations. This will be done by using the complex optical potential, imaginary part of which describes the absorption of the antiproton. Moreover, it would be appropriate to perform calculations with density dependent coupling constants [20, 21], because the density distribution in nuclei with the antiproton varies considerably. The standard RMF models, such as the HS and TM model, do not necessarily have to give a correct results when extrapolated to such high nuclear densities.

Acknowledgement

This work was supported by the GACR grant No. 203/12/2126.

Appendix A

Numerical solution of the equations of motion

We may seek for the static solution of Dirac equation in the form ($\hbar = c = 1$)

$$\psi(x^\mu) = e^{-i\epsilon t}\psi(\vec{x}). \tag{A.1}$$

Then we have

$$\mathcal{H}\psi(x) = E\psi(x), \tag{A.2}$$

where

$$\mathcal{H} = [-i\vec{\alpha}\vec{\nabla} + \beta(m_N + g_{\sigma j}\sigma) + g_{\omega j}\omega_0 + g_{\rho j}\rho_0\tau_3 + e_j\frac{1+\tau_3}{2}A_0]. \tag{A.3}$$

is the single-particle Dirac Hamiltonian. The field operator $\psi(\vec{x})$ can be expanded using positive $u_\beta(\vec{x})$ and negative $v_\beta(\vec{x})$ energy solutions as

$$\psi(\vec{x}) = \sum_\beta \hat{a}_\beta u_\beta(\vec{x}) + \hat{b}^\dagger_\beta v_\beta(\vec{x}) \tag{A.4}$$

in the Schrödinger picture. The operators $\hat{a}_\beta$ and $\hat{b}^\dagger_\beta$ are the annihilation and creation operators for baryons and antibaryons, respectively. They fulfill the well-known anticommutation relations for fermions. The index β involves the full set of quantum numbers describing the single-particle solution. Since the system is assumed spherically symmetric and parity conserving, β contains the usual angular momentum and parity quantum numbers. Since the Dirac Hamiltonian (A.3) is linear in $\vec{p}$, it does not commute with angular momentum $\vec{L}$. It also does not commute with spin operator $\vec{S} = \vec{\Sigma}/2$. But, if we define single-particle angular momentum operator as

$$\vec{J} = \vec{L} + \vec{S}, \tag{A.5}$$

it is easy to show that (A.3) is rotationally invariant, i.e.

$$[\mathcal{H}, J_i] = [\mathcal{H}, \vec{J}^2] = 0 \quad \text{for} \quad i = 1, 2, 3. \tag{A.6}$$

Thus the quantum numbers j and m of angular momentum could be used to label the states. Since Hamiltonian (A.3) obeys $[\mathcal{H}, \vec{S}^2] = 0$, the spin $s = 1/2$ is a constant of the motion. Moreover, by defining the operator

$$\mathcal{K} = \gamma^0[\vec{\Sigma}.\vec{J} - 1/2] = \gamma^0[\vec{\Sigma}.\vec{L} + 1] \tag{A.7}$$

it is straightforward to show that $[\mathcal{H}, \mathcal{K}] = 0$, which provides another constant of the motion. This is a consequence of parity conservation. The eigenvalues of the operator $\mathcal{K}$ are

$$-\kappa = \pm(j + 1/2), \tag{A.8}$$

where κ is a non-zero integer, since

$$\mathcal{K}^2 = \vec{L}^2 + \vec{\Sigma}.\vec{L} + 1 = \vec{J}^2 + 1/4. \tag{A.9}$$

For the upper and lower two-component of the wave function defined as

$$\psi = \begin{pmatrix} \psi_A \\ \psi_B \end{pmatrix} \tag{A.10}$$

it holds:

$$\mathcal{K}\psi = -\kappa\psi = \begin{pmatrix} -\kappa\psi_A \\ -\kappa\psi_B \end{pmatrix} = \begin{pmatrix} (\vec{\sigma}.\vec{L} + 1)\psi_A \\ -(\vec{\sigma}.\vec{L} + 1)\psi_B. \end{pmatrix} \tag{A.11}$$

Consequently, ψ_A and ψ_B are eigenstates of $(\vec{\sigma}.\vec{L}+1)$ with opposite eigenvalues. For $\vec{L}^2 = \vec{J}^2 - \vec{\sigma}.\vec{L} - 3/4$, we obtain

$$\begin{aligned} \vec{L}^2\psi_A &= [(j + 1/2)^2 + \kappa]\psi_A \equiv l_A(l_A + 1)\psi_A \\ \vec{L}^2\psi_B &= [(j + 1/2)^2 + \kappa]\psi_B \equiv l_B(l_B + 1)\psi_B. \end{aligned} \tag{A.12}$$

It implies that upper and lower components are separately eigenstates of $\vec{L}^2$, although ψ is not. For given values of j and κ, the value of l may be determined from

$$\begin{aligned} j(j + 1) - l_A(l_A + 1) + 1/4 &= -\kappa \\ j(j + 1) - l_B(l_B + 1) + 1/4 &= \kappa. \end{aligned} \tag{A.13}$$

The two-component wave functions have fixed j and $s = 1/2$, therefore, l_A and l_B must be $j \pm 1/2$. Their angular momentum and spin parts are spin spherical harmonics

$$\begin{aligned} \Phi_{\kappa m} &= \sum_{m_l m_s} \langle l m_l 1/2 m_s | l 1/2 j m \rangle \, Y_{l m_l}(\theta, \phi) \chi_{m_s} \\ j = |\kappa| - 1/2, \qquad l &= \begin{cases} \kappa & \kappa > 0 \\ -(\kappa+1) & \kappa < 0, \end{cases} \end{aligned} \tag{A.14}$$

where Y_{lm_l} is a spherical harmonic and χ_{m_s} is a two-component Pauli spinor. As a result, the single-particle wave function in a central, parity conserving field may be written as

$$\psi_j^\alpha(\vec{x}) = \psi_j^{n\kappa m t}(\vec{x}) = \begin{pmatrix} i[G_j^{n\kappa t}(r)/r]\Phi_{\kappa m} \\ -[F_j^{n\kappa t}(r)/r]\Phi_{-\kappa m} \end{pmatrix} \zeta_t, \tag{A.15}$$

where ζ_t is a two-component isospinor and G_j^α and F_j^α are the large and small components of the Dirac spinor ($j = N, \overline{N}$). Because of parity conservation, the states may be labeled by their charge or isospin projection t ($t = 1/2$ for protons and $t = -1/2$ for neutrons). The principal quantum number is denoted by n. The phase choice in (A.15) leads to real bound-state wave-functions G_j^α and F_j^α for real potentials in (A.2). Once we have a general form of the solution (A.15), we may evaluate the local meson source terms in the meson field equations. We assume that nuclear ground state consists of filled shells up to some value of n and κ. This is consistent with spherical symmetry and is appropriate for doubly magic nuclei. We also assume that all bilinear products of baryon operators are normal ordered. With these assumptions, the nucleon density becomes

$$\begin{aligned} \rho_N(\vec{x}) &= \langle \underline{F} | : \psi^\dagger(\vec{x}) \psi(\vec{x}) : | \underline{F} \rangle \\ &= \sum_\beta u_\beta^\dagger(\vec{x}) u_\beta(\vec{x}) \\ &= \sum_\alpha \left(\frac{2j_\alpha + 1}{4\pi r^2} \right) (|G_N^\alpha(r)|^2 + |F_N^\alpha(r)|^2), \end{aligned} \tag{A.16}$$

where $|\underline{F}\rangle$ is the filled-shell ground state, the colons imply that $\psi^\dagger\psi$ is normal ordered, and α run over filled shells. With these results, we can rewrite the meson

field equations (2.4) as

$$\left(\frac{d^2}{dr^2}+\frac{2}{r}\frac{d}{dr}-m_\sigma^2\right)\sigma(r) = g_{\sigma N}\rho_S + g_2\sigma + g_3\sigma^2 + \xi\, g_{\sigma N}\rho_{S\bar{p}} \tag{A.17}$$
$$= g_{\sigma N}\sum_\alpha \left(\frac{2j_\alpha+1}{4\pi r^2}\right)(|G_N^\alpha(r)|^2 - |F_N^\alpha(r)|^2)$$
$$+ \xi\, g_{\sigma N}\left(\frac{1}{4\pi r^2}\right)(|G_{\bar{p}}(r)|^2 - |F_{\bar{p}}(r)|^2)$$
$$+ g_2\sigma + g_3\sigma^2$$

$$\left(\frac{d^2}{dr^2}+\frac{2}{r}\frac{d}{dr}-m_{\omega_0}^2\right)\omega_0(r) = -\, g_{\omega N}\rho_V + \xi\, g_{\omega N}\rho_{V\bar{p}} + d\omega_0^3 \tag{A.18}$$
$$= -\, g_{\omega N}\sum_\alpha \left(\frac{2j_\alpha+1}{4\pi r^2}\right)(|G_N^\alpha(r)|^2 + |F_N^\alpha(r)|^2)$$
$$+ \xi\, g_{\omega N}\left(\frac{1}{4\pi r^2}\right)(|G_{\bar{p}}(r)|^2 + |F_{\bar{p}}(r)|^2)$$
$$+ d\omega_0^3$$

$$\left(\frac{d^2}{dr^2}+\frac{2}{r}\frac{d}{dr}-m_\rho^2\right)\rho_0(r) = -\, g_{\rho N}\rho_I - \xi\, g_{\rho N}\rho_{I\bar{p}} \tag{A.19}$$
$$= -\, g_{\rho N}\sum_\alpha \left(\frac{2j_\alpha+1}{4\pi r^2}\right)(|G_N^\alpha(r)|^2 + |F_N^\alpha(r)|^2)(-1)^{t_\alpha-1/2}$$
$$- \xi\, g_{\rho N}\left(\frac{1}{4\pi r^2}\right)(|G_{\bar{p}}(r)|^2 + |F_{\bar{p}}(r)|^2)(-1)^{t_{\bar{p}}-1/2}$$

$$\left(\frac{d^2}{dr^2}+\frac{2}{r}\frac{d}{dr}\right)A_0(r) = -\, e\rho_p + e\rho_{\bar{p}} \tag{A.20}$$
$$= -\, e\sum_\alpha \left(\frac{2j_\alpha+1}{4\pi r^2}\right)(|G_N^\alpha(r)|^2 - |F_N^\alpha(r)|^2)(t_\alpha+1/2)$$
$$+ e\left(\frac{1}{4\pi r^2}\right)(|G_{\bar{p}}(r)|^2 + |F_{\bar{p}}(r)|^2)(t_{\bar{p}}+1/2).$$

The equations for the (anti)nucleon wave functions are obtained by substituting (A.15) into (A.2)

$$\frac{d}{dr}G_j^\alpha(r) + \frac{\kappa}{r}G_j^\alpha(r) - [\epsilon_j^\alpha - g_{\omega j}\omega_0 - t_a g_{\rho j}\rho_0(r) - (t_\alpha + 1/2)e_j A_0(r) + m_j - g_\sigma \sigma_0(r)]F_j^\alpha(r) = 0 \tag{A.21}$$

$$\frac{d}{dr}F_j^\alpha(r) - \frac{\kappa}{r}F_j^\alpha(r) + [\epsilon_j^\alpha - g_{\omega j}\omega_0(r) - t_a g_{\rho j}\rho_0(r) - (t_\alpha + 1/2)e_j A_0(r) - m_j + g_{\sigma j}\sigma_0(r)]G_j^\alpha(r) = 0\ . \tag{A.22}$$

The normalization condition that yields unit probability for finding each particle somewhere in space is

$$\int_0^\infty dr(|G_j^\alpha(r)|^2 + |F_j^\alpha(r)|^2) = 1 \tag{A.23}$$

The equations (A.17) - (A.22) are coupled nonlinear differential equations that can be solved by an iterative procedure. For a given set of meson fields, the Dirac equations (A.21) and (A.22) are solved by Runge-Kutta algorithm integrating outward from the origin and inward from the large r, matching the solutions at some intermediate radius to determine the eigenvalues ϵ_j^α. Analytic solutions in the regions of small and large r allow the proper boundary conditions to be imposed. Once the baryon wave functions are determined, the source terms may be calculated and the meson fields recomputed by integrating over the static Green's function

$$D(r, r'; m_i) = \frac{-1}{m_i r r'} \sinh(m_i r_<) \exp(-m_i r_>). \tag{A.24}$$

This Green's function embodies the boundary conditions for exponential decay at large r and vanishing slope for the fields at origin. For example, the solution of eq. (A.17) for the scalar field reads

$$\sigma_0(r) = \int_0^\infty r'^2 dr'[-g_{\sigma N}\rho_S(r')]D(r, r'; m_\sigma). \tag{A.25}$$

The new meson fields are used to compute the potentials entering the Dirac equations. The solutions of the Dirac equations yield the new spinors for the next iteration. This procedure is repeated until the self-consistency is reached. The total

energy of the system can be expressed as

$$\begin{aligned} E = \langle \underline{F}|\mathcal{H}|\underline{F}\rangle = \int d^3x (\frac{1}{2}[(\nabla\sigma_0)^2 + m_\sigma^2\sigma_0^2] - \frac{1}{2}[(\nabla\omega_0)^2 + m_\omega^2 + \omega_0^2] \\ - \frac{1}{2}(\nabla A_0)^2 - \frac{1}{2}[(\nabla\rho_0)^2 + m_\rho^2\rho_0^2] + \langle \underline{F}| : \psi^\dagger[-i\vec{\alpha}.\vec{\nabla} + \beta(m_N + g_{\sigma j}\sigma_0) \\ + g_{\omega j}\omega_0 + g_{\rho j}\rho_0\tau_3 + e_j\frac{1+\tau_3}{2}A_0]\psi : |\underline{F}\rangle) \end{aligned} \tag{A.26}$$

The part involving the baryon fields can be evaluated using the Dirac equation (A.3)

$$\int d^3x \sum_\alpha \epsilon_j^\alpha \left(\frac{2j_\alpha + 1}{4\pi r^2}\right)(|G_j^\alpha(r)|^2 + |F_j^\alpha(r)|^2) = \sum_\alpha \epsilon_j^\alpha(2j_\alpha + 1). \tag{A.27}$$

For the meson terms, the exponential decay of the fields at large r permits the following partial integration:

$$\begin{aligned} \int d^3x \frac{1}{2}[(\nabla\sigma_0)^2 + m_\sigma^2\sigma_0^2] &= \frac{1}{2}\int d^3x[\sigma_0(-\nabla^2 + m_\sigma^2)\sigma_0] \\ &= \frac{1}{2}\int d^3x g_\sigma \rho_S(r)\sigma_0(r), \end{aligned} \tag{A.28}$$

where the final equality follows from equation (A.17). Similarly, we can rewrite the other terms and express the energy as

$$\begin{aligned} E = &\sum_\alpha \epsilon_j^\alpha(2j_\alpha + 1) + \epsilon_{\bar{p}} \\ &- \frac{1}{2}\int \mathrm{d}^3x\ (-g_{\sigma j}\,\sigma\rho_S + g_{\omega j}\,\omega_0\rho_V + g_{\rho j}\,\rho_0\rho_I + e_j\,A_0\rho_p) \\ &- \frac{1}{2}\int \mathrm{d}^3x\ (-\tfrac{1}{3}g_2\,\sigma^3 - \tfrac{1}{2}g_3\,\sigma^4 + \tfrac{1}{2}d\,\omega^4) \\ &- \frac{1}{2}\int \mathrm{d}^3x\ (-g_{\sigma\bar{p}}\,\sigma\rho_{S\bar{p}} + g_{\omega\bar{p}}\,\omega_0\rho_{V\bar{p}} + g_{\rho\bar{p}}\,\rho_0\rho_{I\bar{p}} - e\,A_0\rho_{\bar{p}}). \end{aligned} \tag{A.29}$$

Bibliography

[1] G. E. Walker, Ch. D. Goodman and C. Olmer, *Antinucleon– and Nucleon–Nucleus Interaction*, Plenum Press 1985

[2] J.-M. Richard, *Antiproton-Nucleus Interaction*, Proc. 1st workshop on antimatter physics at low energy, Fermilab, 10 - 12 April 1986, p.309.

[3] C.J. Batty, E. Friedman, A. Gal, Phys. Rep. **287** (1997) 385.

[4] E. Friedman, A. Gal, Phys. Rep. **452** (2007) 89.

[5] E. Friedman, A. Gal, J. Mareš, Nucl. Phys. **A 761** (2005) 283.

[6] T.J. Bürvenich, W. Greiner, I.N. Mischustin, L.M. Satarov, H. Stöcker, Phys. Rev. **C 71** (2005) 035201.

[7] A.B. Larionov, I.N. Mischustin, L.M Satarov, W. Greiner, Phys. Rev. **C 78** (2008) 014604.

[8] A.B. Larionov, I.N. Mischustin, I.A. Pschenichnov, L.M. Satarov, W. Greiner, Acta Phys.Polon. **B 41** (2010) 299.

[9] T. Bürvenich, I.N. Mischustin, L.M. Satarov, J.A. Maruhn, H. Stöcker, W. Greiner, Phys.Lett. **B 542** (2002) 261.

[10] T. Gaitanos, M. Kaskulov, H. Lenske, Phys. Lett. **B 703** (2011) 193.

[11] X. Chen, N. Li, H. Yao, X. Qin, S. Wu, Commun. Theor. Phys. (Bejing, China) **53** (2010) 128.

[12] The GiBUU model [online]
URL:<http://gibuu.physik.uni-giessen.de/GiBUU> [cit. 18.5.2012]

[13] The PANDA experiment [online]
URL:<http://www-panda.gsi.de/> [cit. 18.5.2012]

[14] J. Hrtánková, *Interaction of antiprotons with nuclei*: Bachelor Thesis. Prague: Czech Technical University in Prague, Faculty of Nuclear Sciences and Physical Engineering, 2011.

[15] B.D. Serot, J.D. Walecka, *Advances in nuclear physics*. Vol. 16, Plenum Press 1986.

[16] B.D. Serot, J.D. Walecka, Int. J. Mod. Phys. E6 (1996) 515.

[17] P.-G. Reinhardt, Rep. Prog. Phys. **52** (1989) 439.

[18] C.J. Horowitz, B.D. Serot, Nucl. Phys. **A 368** (1981) 503.

[19] Y. Sugahara, H. Toki, Nucl. Phys. **A 579** (1994) 557.

[20] S. Typel, H.H. Wolter, Nucl. Phys **A 656** (1999) 331.

[21] C. Fuchs, H. Lenske, H.H. Wolter, Phys. Rev. **C 52** (1995) 6.